HHS Public Access

Author manuscript

Phys Rev Lett. Author manuscript; available in PMC 2014 March 18.

Published in final edited form as:

Phys Rev Lett. 2014 January 10; 112(1): 014302.

Photo-imprint Photoacoustic Microscopy for Three-dimensional Label-free Sub-diffraction Imaging

Junjie Yao, **Lidai Wang**, **Chiye Li**, **Chi Zhang**, and **Lihong V. Wang***

Optical Imaging Laboratory, Department of Biomedical Engineering, Washington University in St. Louis, St. Louis, MO 63130, USA

Abstract

Sub-diffraction optical microscopy allows the imaging of cellular and subcellular structures with resolution finer than the diffraction limit. Here, combining the absorption-based photoacoustic effect and intensity-dependent photobleaching effect, we demonstrate a simple method for sub-diffraction photoacoustic imaging of both fluorescent and non-fluorescent samples. Our method is based on a double-excitation process, where the first excitation pulse partially and inhomogeneously bleaches the molecules in the diffraction-limited excitation volume, thus biasing the signal contributions from a second excitation pulse striking the same region. The differential signal between the two excitations preserves the signal contribution mostly from the center of the excitation volume, and dramatically sharpens the lateral resolution. Moreover, due to the nonlinear nature of the signal, our method offers inherent optical sectioning capability, which is lacking in conventional photoacoustic microscopy. By scanning the excitation beam, we performed three-dimensional sub-diffraction imaging of varied fluorescent and non-fluorescent species. As any molecules have absorption, this technique has the potential to enable label-free sub-diffraction imaging, and can be transferred to other optical imaging modalities or combined with other sub-diffraction methods.

In recent years, by breaking the diffraction limit, sub-diffraction optical microcopy has revolutionized fundamental biological studies. Generally speaking, sub-diffraction techniques fall into two broad categories: so called ‘pattern excitation’ approaches and single-molecule localization approaches [1]. In the method we describe here, the resolution enhancement is based on the excitation nonlinearity of the photobleaching effect, a common phenomenon in optical imaging which is otherwise regarded as harmful [2, 3]. The photobleaching effect depends strongly on the excitation intensity for both fluorescent and non-fluorescent species, which enables sub-diffraction imaging by spatially trimming the excitation volume to a sub-diffraction size [4–6]. Since all molecules are optically absorbing at selected wavelengths, photoacoustic (PA) imaging, which acoustically probes optical absorption contrast in biological tissue, can potentially image all molecules, endogenous and

*Correspondence to: lhwang@wustl.edu.

The other authors declare no competing financial interests.

Additional information

Supplementary information is available in the online version of the paper.

exogenous [7]. Therefore, the combination of the photobleaching effect and photoacoustic imaging can potentially achieve sub-diffraction imaging over a wide-range of species.

Photoacoustic imaging is based on the photoacoustic effect. The principle of photobleaching-based photo-imprint sub-diffraction PA microscopy (PI-PAM) is illustrated in Fig. 1a. When a Gaussian-shape diffraction-limited excitation spot strikes on densely distributed absorbers, the generated PA signal is a summation of the contributions from all absorbers inside the excitation spot (Fig. 1a, left panel). After the first excitation, the absorbers inside the excitation spot are inhomogeneously bleached, depending on the local excitation intensity (Fig. 1a, middle panel). Therefore, the reduction of absorption in the center of the excitation spot is greater than that in the periphery. As a result, when the second pulse excites the same region, the center portion contributes less to the second PA signal than the periphery. The difference between the two PA signals not only reflects the excitation intensity profile, but also incorporates the absorption reduction distribution (Fig. 1a, right panel), which therefore sharpens the center of the focus. This concept of enhancement in the lateral resolution is elucidated in Fig. 1b. In summary, while each PA signal is linear to the excitation intensity, the differential signal is nonlinear to the excitation intensity. This is the physical basis of our method.

The contrast of the PI-PAM comes from the differential signal between two adjacent frames, expressed as (see Supplementary Note 1 for more derivation)

$$\Delta P = P_{i-1} - P_i \propto k\Gamma\eta_{\mathrm{th}} N_0 I^{b+1}, \quad (1)$$

where P_i is the signal amplitude detected by the ultrasonic transducer with the i th excitation, Γ is the Grueneisen coefficient, η_{th} is the percentage of the absorbed photon energy that is converted into heat, N_0 is the initial number of molecules, I is the excitation intensity, and b is the power dependence of the photobleaching rate on the excitation intensity. Eq. 1 indicates that, on the one hand, the PI-PAM signal is linear to the optical absorption, which maintains its functional imaging capability, such as oxygen saturation measurement. On the other hand, the PI-PAM signal is nonlinear to the excitation intensity, which enables sub-diffraction imaging capability.

If the excitation profile can be approximated by a Gaussian function, we obtain the full-width-at-half-maximum (FWHM) of the lateral point spread function (PSF) of the imaging system as (see Supplementary Note 2 for more detailed derivation)

$$FWHM_r = \sqrt{\frac{2\ln 2}{1+b}} w_e \approx \frac{0.51}{\sqrt{1+b}} \frac{\lambda_0}{NA}, \quad (2)$$

where r is the radial distance from the center of the Airy disk, w_e is the Gaussian width of the excitation beam where the beam intensity drops to $1/e^2$ of its center value, λ_0 is the excitation wavelength and NA is the numerical aperture of the objective. Eq. 2 indicates that, the effective PSF (Fig. 1b, right panel) of the system is sharper than the initial diffraction-limited excitation PSF (Fig. 1b, left panel) by a factor of $\sqrt{1+b}$.

Similarly, the axial resolution of PI-PAM for point targets is given by the FWHM of the axial PSF as (see Supplementary Note 3 for more detailed derivation)

$$FWHM_z^{\text{point}}=2\sqrt{2^{1/(1+b)}-1}z_R=1.8\sqrt{2^{1/(1+b)}-1}\frac{\lambda_0}{NA^2}, \quad (3)$$

where z is the axial distance from the focal plane, Z_R is the Rayleigh range of the Gaussian beam. Eq. 3 shows that, by sharpening the optical focal zone, PI-PAM provides an axial resolution improvement by a factor of $1/\sqrt{2^{1/(1+b)}-1}$ over conventional PAM for point targets.

For planar (or wide) targets, conventional PAM lacks sectioning capability because its axial PSF is constant. By contrast, for PI-PAM, the optical sectioning capability can be expressed as the FWHM of the axial PSF:

$$FWHM_z^{\text{planar}}=2\sqrt{2^{1/b}-1}z_R=1.8\sqrt{2^{1/b}-1}\frac{\lambda_0}{NA^2}. \quad (4)$$

Eq. 4 shows that the optical sectioning capability of PI-PAM also depends on the intensity power dependence of the photobleaching rate.

The photo-imprint PA microscopy system is illustrated in Fig. 1c (for more details, see Methods and Supplementary Fig. 1). Briefly stated, an OPO (optical parametric oscillator) laser with a wavelength tuning range of 210–2600 nm serves as the excitation source. After spatial filtering, the beam is focused into the sample by a 1.4 NA (numerical aperture) oil-immersion objective. The photoacoustic waves are detected by a focused ultrasonic transducer (customized with 40 MHz central frequency, 80% bandwidth, and 0.50 NA), which is placed confocally with the objective and coupled by water. A customized Labview program synchronizes the entire system. PI-PAM imaging can be performed point by point (A-scan mode), cross-section by cross-section (B-scan mode), or volume by volume (C-scan mode). If not otherwise mentioned, A-scan mode was used for the experiments in this paper. The second pulse is a separate event, which follows the first pulse that partially bleaches the absorbers. To ensure that the PA signals from two consecutive pulses do not temporally overlap, the time interval between the two pulses should be at least a few microseconds. In practice, we make sure that the two pulses are more than 1 millisecond apart. To achieve sufficient detection sensitivity, typically more than 200 frames were acquired for each experiment.

To improve the signal-to-noise ratio (SNR), in practice, we took the difference between frames that are half of the total number of frames apart, and then averaged all the differential images (Supplementary Note 4 for more detailed derivation). Assume that the total number of frames is M, the true signal difference between adjacent frames is ΔS, and the standard deviation of the white noise is σ. Approximately, averaging of the differential signals between frames that are $M / 2$ apart yields an SNR of

$$SNR_{M/2}=\frac{M}{4}\sqrt{M}\frac{\Delta S}{\sigma}. \quad (5)$$

The SNR ratio between PI-PAM and conventional PAM is given by

$$R_{\mathrm{SNR}}=\frac{SNR_{\mathrm{PI-PAM}}}{SNR_{\mathrm{C-PAM}}}=\frac{q}{2(2-q)}. \quad (6)$$

Eq. 6 suggests that the SNR advantage of conventional PAM decreases as the bleached percentage *q* increases. The SNR of PI-PAM can be improved by increasing the bleaching percentage with either more imaging frames or stronger excitation intensity.

Using this setup, we first studied the photobleaching characteristics of several biological and non-biological samples commonly used in PA imaging, including red blood cells, B16 melanoma cells, black ink, gold nanoparticles, and graphite (Supplementary Fig. 2). An exponential-decay model was used to fit for the photobleaching rate at different excitation intensities. The power dependence of each material on the excitation intensity determines the expected resolution improvement. Among the test materials, gold nanoparticles have the highest power dependence of 4.0, which is expected to improve the lateral resolution to ~87 nm.

The lateral resolution enhancement of PI-PAM over conventional PA microscopy (PAM) is presented in Fig. 2. A sharp blade edge coated with hemoglobin was imaged at 532 nm, and the corresponding line spread function was fitted to compute the lateral resolution (Fig. 2a). With an objective NA of 1.4, conventional PAM achieved a lateral resolution of 200 nm, in agreement with the diffraction limit. By contrast, PI-PAM achieved a sub-diffraction lateral resolution of 120 nm, a 1.7-fold improvement. Since the photobleaching of hemoglobin has a power dependence of 2.2 on the excitation intensity, the measured resolution is close to the expected value of 112 nm. To demonstrate the imaging performance, conventional PAM and PI-PAM were applied to image a monolayer of 200-nm-diameter densely packed red-dyed microspheres (Fig. 2b). The red dye's photobleaching property was similar to that of hemoglobin. The images show that the microspheres were much better resolved by PI-PAM, which confirmed the lateral resolution improvement.

We further demonstrate the sub-diffraction imaging capability of PI-PAM on both non-biological and biological samples (Fig. 3). We compared conventional PAM and PI-PAM images of 150-nm-diameter gold nanoparticles (Fig. 3a, Movie S1). Two closely located nanoparticles, 270 nm apart, were clearly resolved by PI-PAM but barely resolved by conventional PAM (Fig. 3a, insets). The line profile across one nanoparticle shows a full-width-at-half-maximum of 170 nm (Fig. 3a, right). Because the line profile is a convolution of the effective PSF of the system with the particle absorption profile, deconvolution of the line profile using the Gaussian approximation results in an effective lateral resolution of 80 nm for PI-PAM, consistent with the expected value. We also imaged a fixed B16 melanoma cell (Fig. 3b, and Movie S2). The PI-PAM image is clearly superior in resolution. Small

dendrites in the melanoma cell that are less than 100 nm apart can be clearly separated by PI-PAM (Fig. 3b, insets).

The other important advantage offered by PI-PAM is its optical sectioning capability, providing axial resolution for not only point targets but also targets that are large relative to the lateral resolution. As shown by Eq. (4), the axial resolution for planar targets originates from the non-uniform light intensity along the axial beam axis. The light intensity is stronger at the focal plane. Therefore, the absorbers at the focal plane are bleached more than the absorber farther away from the focal plane. The difference of the PA signals before and after bleaching is thus axial position dependent. This dependence results in the axial resolution for planar targets. A simple illustration is shown in Fig. 4a. Like the lateral resolution enhancement, the sectioning strength of PI-PAM is determined by the power dependence of the photobleaching rate on the excitation intensity. For example, with a linear dependence, PI-PAM should achieve sectioning capability comparable with that of confocal microscopy. We first quantified the sectioning by using a layer of dried hemoglobin (~150 nm in thickness) (Fig. 4b, Supplementary Fig. 3). While the signal strength in conventional PAM decayed very slowly, the signal strength in PI-PAM sharply dropped as the sample moved out of focus. The FWHM of the signal profile in PI-PAM suggests a sectioning capability of 370 nm after deconvolution with the absorption profile of the sample, close to the expected value (320 nm). Accordingly, a single layer of red blood cells fixed on a cover glass was imaged at varying axial positions (Fig. 4c, and Movie S3). The stack of the maximum-amplitude projections on the orthogonal plane clearly shows the optical sectioning capability of PI-PAM (Fig. 4c).

Finally, we applied PI-PAM to sub-diffraction imaging of live rose petal epidermal cells at 570 nm. Pink anthocyanins in cell vacuoles provided the absorption contrast for PA imaging, and they are also commonly used for fluorescence imaging (Supplementary Fig. 4). In the PA images, densely packed epidermal cells can be clearly resolved. The cell vacuoles are bright, while the cell walls and cell nuclei are dark (Fig. 4d). By *z*-scanning the sample with a step size of 0.5 μm, PI-PAM was performed to section the cells at different depths (Fig. 4e and 4F, Movie S4). With *z*-scanning, PI-PAM has achieved three-dimensional sub-diffraction resolution.

In summary, we have demonstrated three-dimensional sub-diffraction imaging of both fluorescent and non-fluorescent samples by spatially trimming the excitation volume via the photobleaching effect. We note that PI-PAM can be applied to both fluorescent and non-fluorescent species [8]. When fluorescence is present, it may change the bleaching rate power dependence on the excitation intensity, and thus the resolution improvement. Fortunately, most fluorescent species have a quite low quantum yield (typically less than 10%), therefore, the non-fluorescent bleaching effect still dominates the imaging process.

It is necessary to discuss the bleaching effect on the relative feature contrast between the ‘bleached region’ and ‘non-bleached region’. First, approximately, only the absorbers within the optical focal plane are bleached. When the optical focal plane is moved to other depths, the same bleaching process is repeated and thus the final image contrast between different depths should not be changed. Second, the distortion between the ‘bleached’ and ‘non-

bleached' regions can be minimized by reducing the frame numbers or the excitation light intensity. However, this results in reduced SNR as well. In practice, a balance between sample distortion and SNR should be carefully determined. If permanent photobleaching is a concern in the imaging process, the dynamics of reversibly photoswitchable chromophores can be used instead. While the photoswitchable chromophores can be cycled between bright and dark states, the switching rate strongly depends on the switching light intensity [9, 10], which provides a zero-loss alternative for PI-PAM.

The same principle of PI-PAM can be readily transferred to fluorescence microscopy, the major imaging tool currently used in biological studies. Because the photobleaching effect occurs in the excitation phase of the imaging process, our method can be applied to confocal microscopy and two-photon microscopy. Compared with other optical imaging modalities, PA detection is not necessary superior, because each modality has its own unique advantages. Our main purpose is to introduce a sub-diffraction imaging method to both PA and other optical imaging communities. Compared with fluorescence microscopy, photoacoustic microscopy can image non-fluorescent species, and can potentially penetrate deeper due to the one-way optical scattering. However, compared with optical imaging where high sensitivity detectors are used, PA imaging suffers from the relatively low SNR due to the less sensitive ultrasonic transducers. To further improve the PA detection sensitivity, more work is necessary to develop optimum illumination and state-of-the-art acoustic detectors [11]. We expect that realizable improvements to the acoustic detector may enable single molecule detection sensitivity, comparable to that of optical detection [11].

Supplementary Material

Refer to Web version on PubMed Central for supplementary material.

Acknowledgements

The authors appreciate Prof. James Ballard's close reading of the manuscript, and also appreciate useful discussions from Konstantin Maslov, Amos Danielli, and Arie Krumholz. This research was supported by the National Institutes of Health Grants DP1 EB016986 (NIH Director's Pioneer Award), R01 EB008085, R01 CA134539, U54 CA136398, R01 CA157277, and R01 CA159959. L. V. Wang has a financial interest in Endra, Inc., and Microphotoacoustics, Inc., which, however, did not support this work.

References

1. Huang B, Bates M, Zhuang XW. Super-Resolution Fluorescence Microscopy. Annual Review of Biochemistry. 2009; 78:993–1016.
2. Jacobson K, et al. Fluorescence Photobleaching in Cell Biology. Nature. 1982; 295(5847):283–284. [PubMed: 7057892]
3. Rasnik I, McKinney SA, Ha T. Nonblinking and longlasting single-molecule fluorescence imaging. Nature Methods. 2006; 3(11):891–893. [PubMed: 17013382]
4. Gao L, et al. Photothermal bleaching in time-lapse photoacoustic microscopy. J Biophotonics. 2013; 6(6–7):543–548. [PubMed: 23184422]
5. Chen TS, et al. High-order photobleaching of green fluorescent protein inside live cells in two-photon excitation microscopy. Biochemical and Biophysical Research Communications. 2002; 291(5):1272–1275. [PubMed: 11883955]
6. Patterson GH, Piston DW. Photobleaching in two-photon excitation microscopy. Biophysical Journal. 2000; 78(4):2159–2162. [PubMed: 10733993]

7. Wang LHV, Hu S. Photoacoustic Tomography: In Vivo Imaging from Organelles to Organs. Science. 2012; 335(6075):1458–1462. [PubMed: 22442475]
8. Launer HF. Photobleaching[mdash]a Common Phenomenon. Nature. 1968; 218(5137):160–161.
9. Bates M, et al. Multicolor super-resolution imaging with photo-switchable fluorescent probes. Science. 2007; 317(5845):1749–1753. [PubMed: 17702910]
10. Subach OM, et al. A photoswitchable orange-to-far-red fluorescent protein, PSmOrange. Nature Methods. 2011; 8(9) 771-U125.
11. Winkler AM, Maslov K, Wang LV. Noise-equivalent sensitivity of photoacoustics. Journal of Biomedical Optics. 2013; 18(9):097003. [PubMed: 24026425]

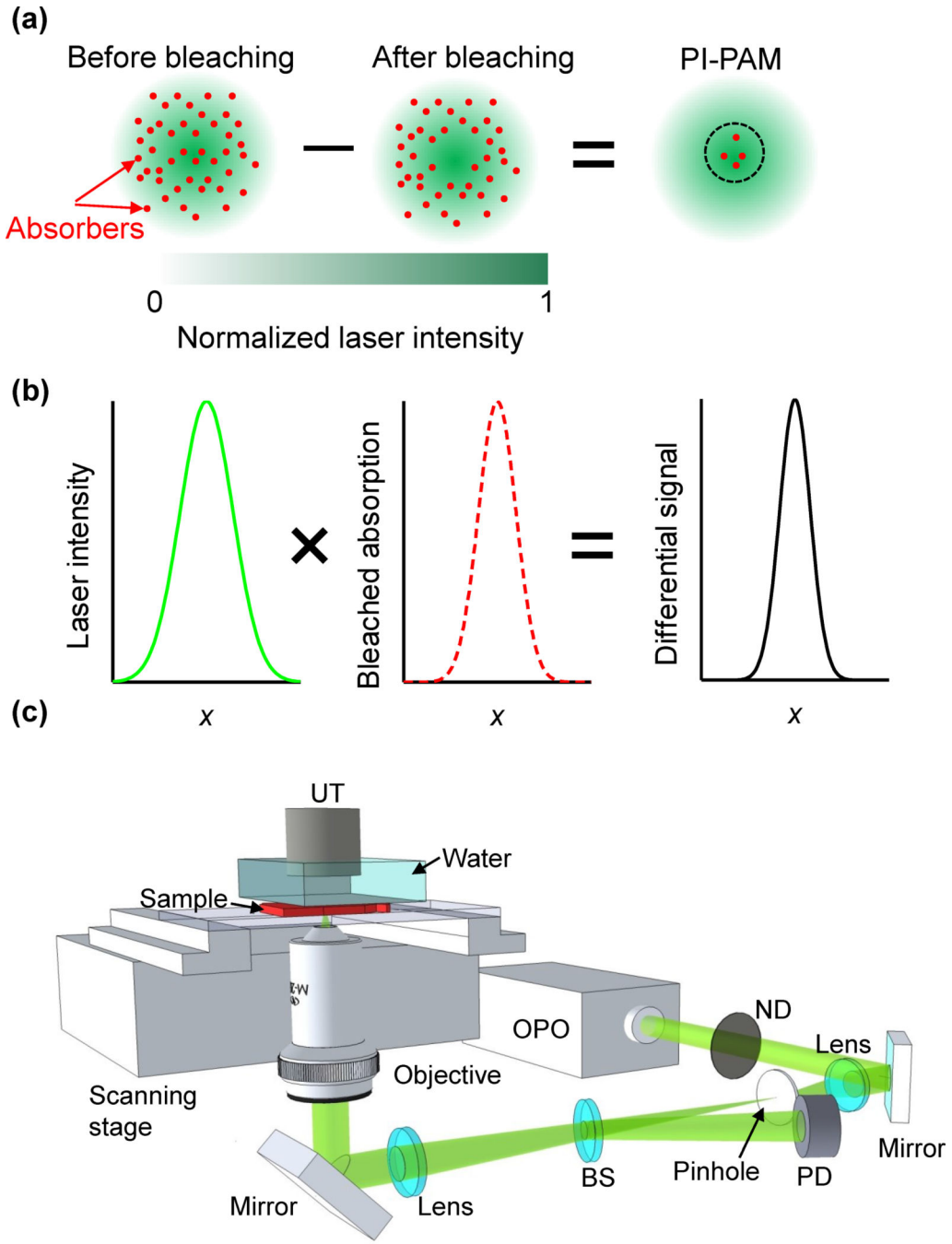

Fig. 1.

Photo-imprint photoacoustic microscopy (PI-PAM). (a) Principle of PI-PAM. The differential signal between before- (left panel) and after-bleaching (middle panel) images results in a smaller effective excitation size, as shown by the dashed circle in the right panel. (b) Illustration of the lateral resolution enhancement by PI-PAM. The effective PSF is the product of the excitation PSF and the photobleaching profile. (c) Schematic of the central components of a PI-PAM system. BS, beam sampler; ND, neutral density filter; OPO, optical parametric oscillator; UT, ultrasonic transducer.

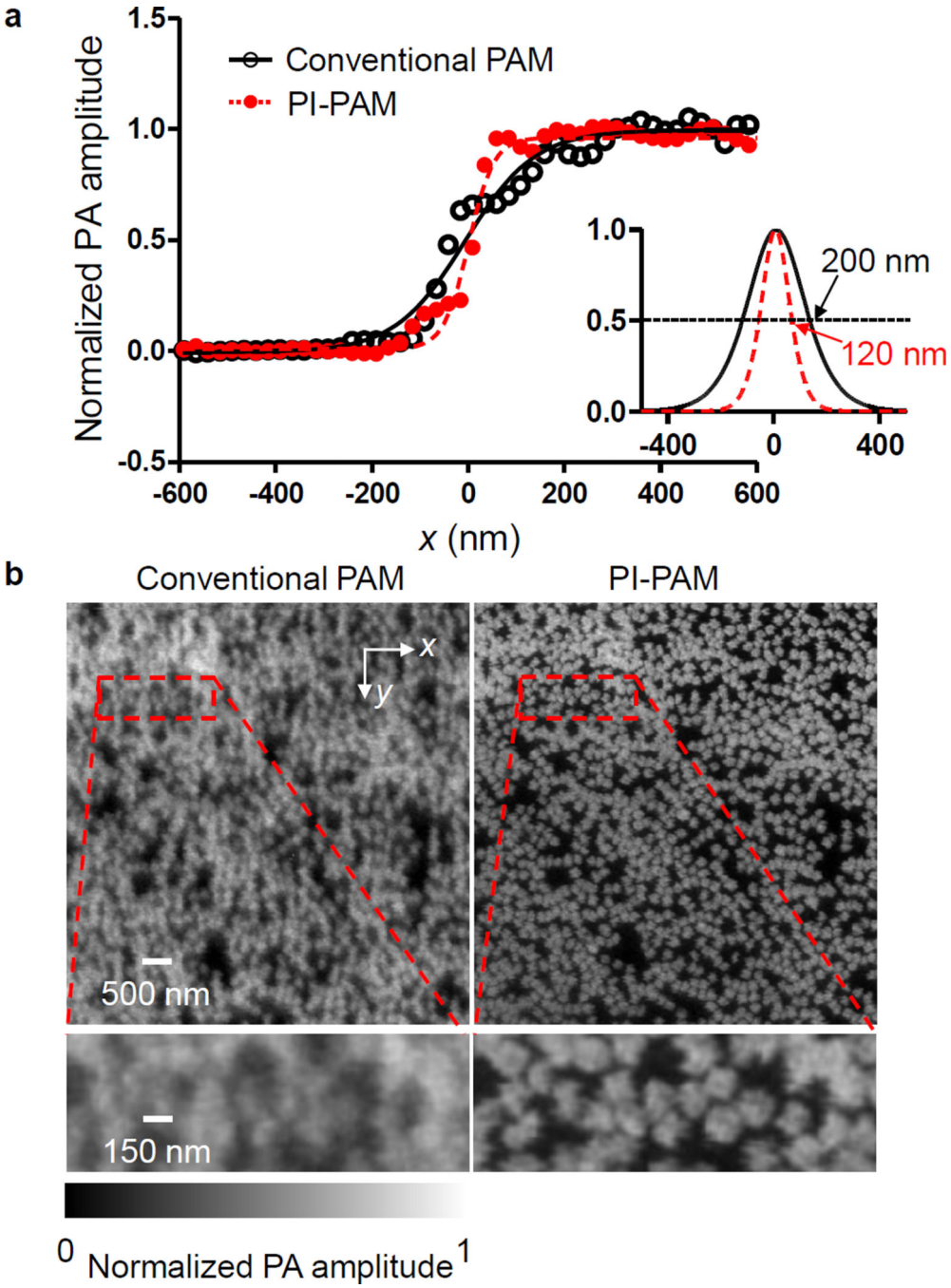

Fig. 2.

Lateral resolution enhancement by PI-PAM. (a) Edge spread function of conventional PAM and PI-PAM, using a sharp blade edge coated with hemoglobin. (b) A cluster of red-dyed microspheres with nominal diameters of 200 nm, as imaged by conventional PAM (left) and PI-PAM (right). The dashed boxes in the top row were magnified and shown in the bottom row.

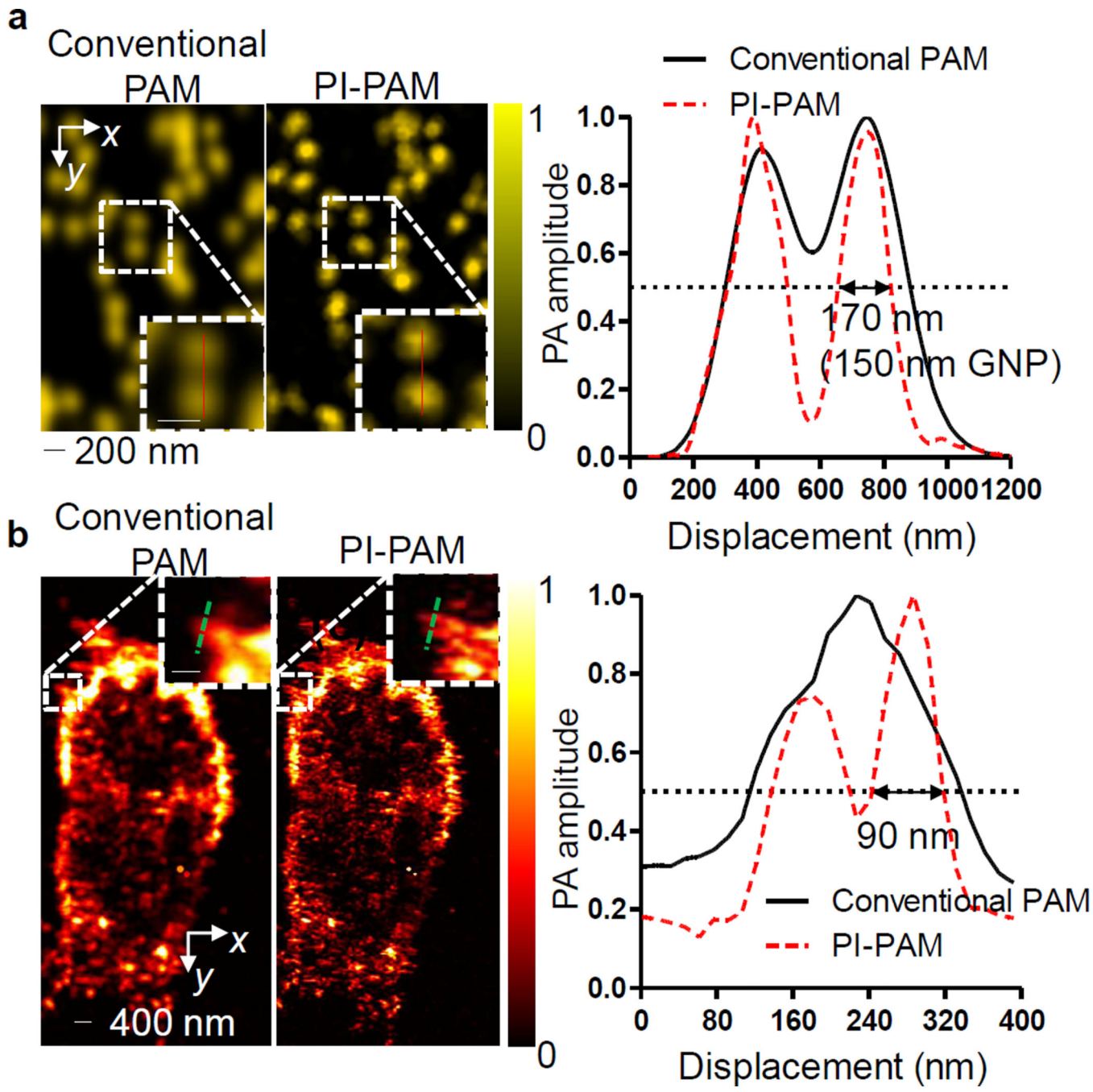

Fig. 3.

PI-PAM imaging of gold nanoparticles and melanoma cells with enhanced lateral resolution. (a–b) 150-nm-diameter gold nanoparticles (a), and a B16 melanoma cell (b) imaged by conventional PAM (left column) and PI-PAM (middle column). The normalized signal amplitude profiles along the dashed lines are shown in the right column. Insets show magnified views of the marked areas. The scale bars for the insets are 200 nm.

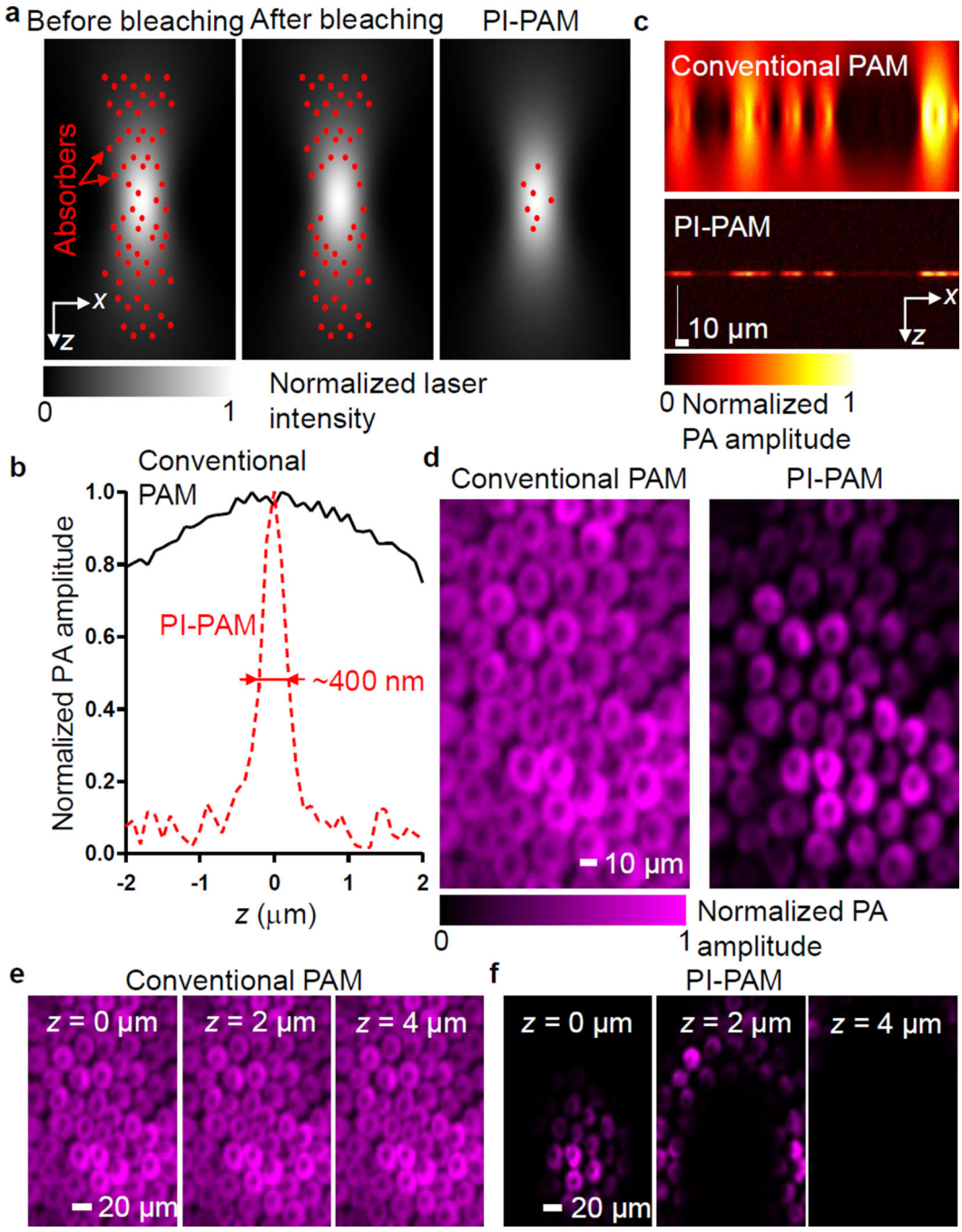

Fig. 4.

Optical sectioning capability of PI-PAM. (a) Illustration of the optical sectioning capability provided by PI-PAM. The differential signal of the before- (left) and after-bleaching (middle) images largely removes the out-of-focus contributions. (b) The axial point spread function measured on a thin-layer hemoglobin sample. (c) Orthogonal projections of single layer red blood cells imaged by conventional PAM and PI-PAM at varying axial positions. (d–f) Sub-diffraction imaging of live rose petal epidermal cells at 570 nm. The sample was

z-scanned with a step size of 0.5 μm. Maximum-amplitude-projections (d) were extracted from the z-stacked images (e–f).